Electrostatic Shaping of Magnetic Transition Regions in $La_{0.7}Sr_{0.3}MnO_3$

Qianqian Lan [1,2,*] Chuanshou Wang,[3] Lei Jin,[1] Michael Schnedler,[1] Lars Freter,[1] Kurt Fischer,[4]
Jan Caron [1] Xian-Kui Wei [1] Thibaud Denneulin [1] András Kovács [1] Philipp Ebert [1]
Xiaoyan Zhong,[5,6,7,†] and Rafal E. Dunin-Borkowski[1]

[1]*Ernst Ruska-Centre for Microscopy and Spectroscopy with Electrons (ER-C 1) and Peter Grünberg Institut (PGI-5),*
Forschungszentrum Jülich GmbH, 52425 Jülich, Germany
[2]*National Center for Electron Microscopy in Beijing, Key Laboratory of Advanced Materials (MOE),*
School of Materials Science and Engineering, Tsinghua University, Beijing 100084, People's Republic of China
[3]*Department of Physics, Southern University of Science and Technology, Shenzhen 518055, People's Republic of China*
[4]*Department of Mechanical and Electrical Engineering, National Institute of Technology,*
Tokuyama College, Gakuendai, Shunan, Yamaguchi, 745-8585, Japan
[5]*TRACE EM Unit and Department of Materials Science and Engineering, City University of Hong Kong,*
Kowloon 999077, Hong Kong SAR, People's Republic of China
[6]*City University of Hong Kong, Shenzhen Futian Research Institute, Shenzhen 518048, People's Republic of China*
[7]*Nanomanufacturing Laboratory, City University of Hong Kong,*
Shenzhen Research Institute, Shenzhen 518057, People's Republic of China

We report a magnetic transition region in $La_{0.7}Sr_{0.3}MnO_3$ with gradually changing magnitude of magnetization, but no rotation, stable at all temperatures below T_C. Spatially resolved magnetization, composition and Mn valence data reveal that the magnetic transition region is induced by a subtle Mn composition change, leading to charge transfer at the interface due to carrier diffusion and drift. The electrostatic shaping of the magnetic transition region is mediated by the Mn valence, which affects both magnetization by Mn^{3+}-Mn^{4+} double exchange interaction and free carrier concentration.

Ferromagnetic (FM) materials naturally form various domains, with different orientations of magnetization, as a result of competition among primarily the exchange interaction, magnetic anisotropy, and stray field energies [1]. The domains, with internally uniform effective magnetization, are separated by domain walls (DW), which are transition regions where the magnetization changes gradually between the adjacent domains. The DWs can be classified according to their internal nanoscale spin structure: Bloch [2] and Néel [3] DWs, where the magnetization rotates out-of plane and in plane, respectively, as well as mixtures of both [4], are most widely occurring. Furthermore, cross-tie [5–8] and chiral DWs [9–11] can occur in thin films and complex vortex style structures in DWs between head-to-head domains in nano-sized ribbons [12–14]. The common feature of all thus far observed magnetic DWs is that the orientation of magnetization rotates gradually, while the magnitude of magnetization remains constant.

In contrast, Bulaevskii and Ginsburg predicted the existence of a magnetic DW without rotation of magnetization, where the transition is achieved by gradual change of the magnitude of magnetization [15,16]. This DW structure, termed in the following Bulaevskii-Ginsburg DW, requires either local spin fluctuations (magnons) [17,18], or that the density of spins and magnetic moments is spatially varying. The former is expected to occur only very close to the Curie

temperature (T_C), where fluctuation of spins can locally reduce the resulting effective magnetization. This corresponds to the initial mechanism predicted by Bulaevskii and Ginsburg [15,16]. The latter has deep implications for ferromagnetic material, as a change in the density of spins is not trivial for classical ferromagnets. In view of this situation, it is no surprise that such a DW has to our knowledge not been observed experimentally yet.

Here we report, however, that in $La_{0.7}Sr_{0.3}MnO_3$ (LSMO) magnetic transition regions exist, where the magnitude of magnetization is gradually changing without rotation, even well below T_C. The change of the magnitude of magnetization is found to be driven by a diffusion and drift-induced charge carrier redistribution, which changes the Mn^{3+}/Mn^{4+} ratio and thereby the density of magnetic moments governed by the Mn^{3+}/Mn^{4+} double exchange interaction mechanism. This Mn valence mediated electrostatic-magnetic coupling lifts the constraint that the Bulaevskii-Ginsburg DW is only stable near T_C, widening the stable temperature range down to 0 K.

The results are demonstrated using a 200-nm-thick epitaxial LSMO film deposited on $SrTiO_3$ (STO) (see Supplemental Material [19] for details). The *macroscopic* magnetization of this LSMO film, measured by a superconducting quantum interference device (SQUID) magnetometer, exhibits two magnetic transition temperatures, a
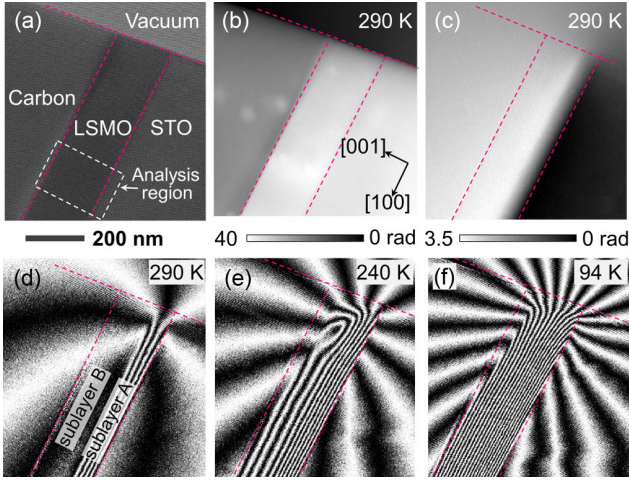
FIG. 1. Off-axis EH results. (a) Representative off-axis electron hologram of the LSMO film on a Nb-doped STO substrate covered by a protective carbon layer with the analysis region marked. (b) Mean inner and electrostatic potential contribution to the phase reconstructed from (a). (c) Reconstructed magnetic phase shift at 290 K with the mean inner and electrostatic potential contribution removed. (d)–(f) Magnetic induction maps with a phase contour spacing of π radians at 290, 240, and 94 K, respectively. The denser are the phase contours in the specimen, the stronger is the magnetization. In the upper left corner of the LSMO layer, focused ion beam damage is present and suppresses ferromagnetism.

FIG. 2. (a) Line profile of the magnetic phase shift φ (black) and its first derivative $d\varphi/dx$ (blue) at 240 K vs distance x in [001] direction through the LSMO film. The orange dashed lines are linear fits. The red line represents a hyperbolic tangent fit using $M(x) = \Delta M \times \tanh(1.76x/w)$ [27], with the amplitude difference ΔM and the full width at half maximum (FWHM) w. The fit is used to smooth the noise in the further analysis and to determine the transition region's width. The gray vertical dashed lines indicate the approximate width of the transition region. (b) Map of projected *in-plane* magnetization M (green arrows) reconstructed from the magnetic phase image at 240 K. The lengths and directions of the arrows indicate the magnitudes and directions of the magnetization.

primary one at 339 K (typical for LSMO films [20–22]) and an additional one at 279 K (Fig. S1, [19]). To understand this behavior, *in situ* off-axis electron holography (EH, see Fig. S2 [19] for details) is used to quantitatively map the spatial fluctuations of magnetization of the LSMO layer in cross-sectional geometry [23].

Figure 1(a) shows a representative electron hologram acquired at 290 K, from which the derived electrostatic or mean inner potential and magnetic contributions to the phase are shown in Figs. 1(b) and 1(c), respectively (Fig. S2, [19,24,25]). The corresponding magnetic induction map is illustrated in Fig. 1(d), where the density and direction of the phase contours represent the strength and direction of the projected *in-plane* magnetic induction within and around the specimen. The magnetic induction map reveals an *in-plane* remanent magnetization M aligned parallel to the LSMO/STO interface, as expected due to a combination of magnetocrystalline and shape anisotropy, as well as magnetizing direction. However, the magnetization is present only in the region adjacent to the STO substrate. With decreasing temperatures, the magnetization extends progressively to the entire thickness of the LSMO film [Figs. 1(e), 1(f)]. The LSMO film can therefore be treated as a bilayer system, consisting of a FM phase in the first ~75 nm from the LSMO/STO interface [denoted sublayer A in Fig. 1(d)] and a paramagnetic (PM) phase in the rest of the layer [denoted sublayer B in Fig. 1(d)]
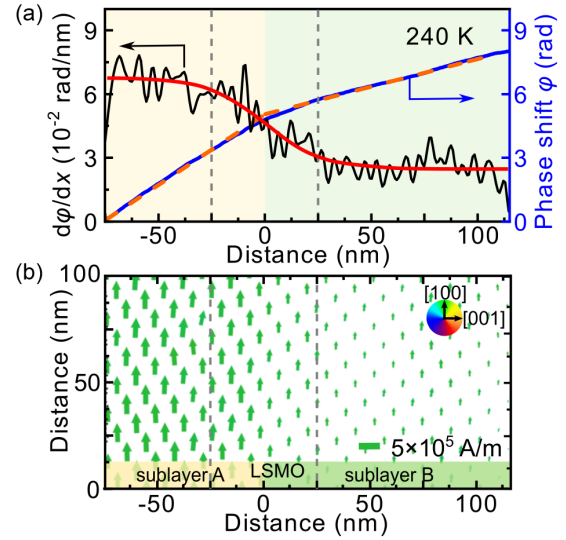
at room temperature. The PM sublayer B becomes FM when the temperature decreases. At 346 K the entire LSMO film shows no detectable magnetic signal, indicating everywhere a PM state. The observation of two distinct LSMO sublayers with different values of T_C explains the presence of two magnetic transition temperatures of 279 and 339 K in the macroscopic magnetization probed by SQUID (Fig. S1, [19]).

In order to map the magnetization distribution in the LSMO film quantitatively, the local projected *in-plane* remanent magnetization M was determined from each magnetic phase image. Figure 2(a) shows the extracted magnetic phase shift and its first derivative at 240 K. Given that the derivative is proportional to the magnetization (assuming a uniform specimen thickness and negligible fringing fields) [23], the consistently positive slope indicates that the *in-plane* magnetization has the same orientation in both sublayers. The change in slope indicates that the magnetization in sublayer A is larger than that in sublayer B, in line with the different magnitudes of the derivative. Figure 2(b) shows the corresponding two-dimensional projected *in-plane* magnetization map, derived using a model-based iterative reconstruction algorithm [26]. It demonstrates an *in-plane* magnetization everywhere parallel to the interface, but with different
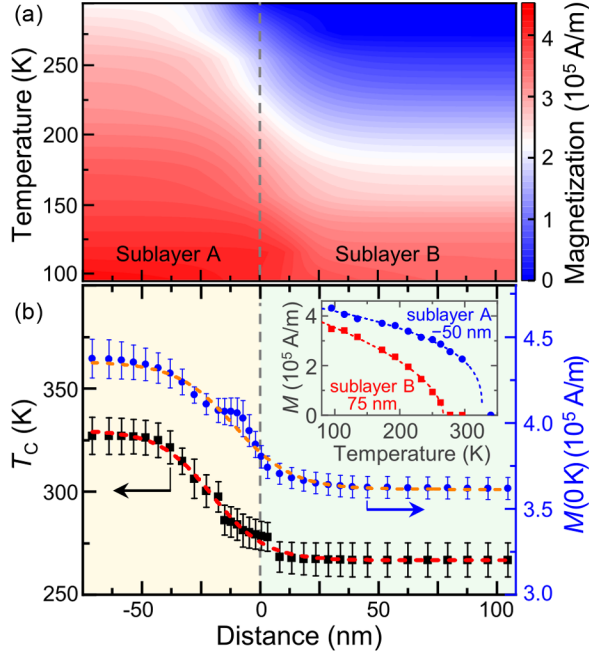
FIG. 3. Remanent magnetization magnitude M and Curie temperature T_C within the LSMO layer. (a) M vs temperature and position in [001] direction. (b) T_C (black squares, left axis) and M at 0 K (blue dots, right axis) vs distance, derived from fits of the temperature dependent magnetization data $M(T)$ [$M(T)$ examples at positions -50 and $+75$ nm with fits are shown in the inset]. The dashed lines in (b) represent fits to $M(0 \text{ K})$ and T_C using the hyperbolic tangent expression of Fig. 2(a).

magnitudes in both sublayers. To determine the out-of-plane magnetization component we performed electron holographic tomography (see Fig. S3, [19]), revealing that the out-of-plane rotation of the magnetization at 94 K is below the detection limit of 1°. Hence, there is *only* an in-plane magnetization present.

The remanent magnetization magnitude M in the LSMO layer, averaged parallel to the LSMO/STO interface, is shown in Fig. 3(a) vs temperature and spatial position. The most prominent feature is that M is larger in sublayer A than in sublayer B at a given temperature, suggesting different values of T_C. The spatial variation of T_C was determined from a series of $M(T)$ curves extracted from Fig. 3(a), by fitting the functional form $M \sim (1 - T/T_C)^n$ to the data [22] [see inset in Fig. 3(b) for examples]. Figure 3(b) reveals two dominant T_C values, 327 ± 9 K (sublayer A) and 267 ± 9 K (sublayer B), in agreement with the macroscopic magnetization data, and a $w_{Tc} = 48 \pm 3$ nm wide transition region in between.

Furthermore, we deduced the magnitude of the magnetization at 0 K, $M(0 \text{ K})$, by fitting the above $M(T)$ data with the functional form $M(T) \approx M(T = 0 \text{ K}) \times [1 - \gamma(T/T_C)^\beta]$ [18,28], with the previously determined T_C. The $M(0 \text{ K})$ data in Fig. 3(b) reveal a similar wide transition region again ($w_{M(0 \text{ K})} = 44 \pm 4$ nm). Since at 0 K

magnons are not excited, they are not relevant for this transition region [18].

The above measurement of the spatial magnetization distribution raises two closely related questions: (i) The origins of the different levels of magnetization in the two sublayers and (ii) the physical effects governing the magnetic transition region. If we turn to classical ferromagnetic materials, the DW's width w at the boundary between two magnetic domains is determined by a balance between exchange energy (increasing w) and magnetocrystalline anisotropy (decreasing w) [1]. However, in our case the confining effect of the magnetocrystalline anisotropy energy is absent, due to the parallel magnetization everywhere. Only its magnitude is changing. Hence, the transition region would be expected to widen infinitely to lower the exchange interaction energy. Since this is not the case, there has to be a different physical mechanism governing magnetic transition regions in LSMO.

In order to deduce this physical mechanism, first, the lattice constants in each sublayer were measured using selected area electron diffraction and atomic-resolution high-angle annular dark-field scanning TEM. The results in Fig. S4 [19] indicate that there is no measurable change in structure and biaxial strain between the LSMO sublayers, eliminating in our case lattice or phase changes [29].

Second, the normalized elemental compositions measured in the [001] growth direction by energy-dispersive x-ray (EDX) spectroscopy and electron energy-loss spectroscopy (EELS) [Fig. 4(a)] show that the Sr, La, and O compositions remain constant at average values of 0.294 ± 0.002, 0.706 ± 0.002, and 2.99 ± 0.01 consistent with the intended stoichiometry of $La_{0.7}Sr_{0.3}MnO_3$. However, the $[Mn]/([La] + [Sr])$ ratio decreases from sublayer A to sublayer B, indicating a Mn deficiency in sublayer B with respect to sublayer A of $4.3 \pm 1.1\%$ [confirmed by secondary ion mass spectrometry (SIMS) yielding a drop of $3.0 \pm 0.3\%$]. The average FWHM of the Mn concentration change is 7 ± 4 nm.

Third, a change in Mn concentration is expected to be accompanied by a change in Mn valence state, in order to maintain charge neutrality. This is corroborated by the Mn L_3/L_2 edge ratio measured using EELS [Fig. 4(b)], decreasing from sublayer A to sublayer B with a FWHM of the transition region of $w_{EL} = 61 \pm 6$ nm. First, we focus only on the values far away from the transition region: The result shows that the Mn valence state is higher in sublayer B than in sublayer A by $\Delta V = 0.136 \pm 0.028$, obtained by using the linear dependence of the L_3/L_2 ratio on valence state with a slope of -0.73 ± 0.11 [30,31]. This ΔV value can be compared with a calculation based on the measured Mn composition change δ in $(La_{0.7}Sr_{0.3})^{2.7} Mn_{1-\delta}^{3.3+\Delta V}(O_3)^{-6}$, assuming charge neutrality and that valence states and compositions of Sr, La, and O are unchanged. This yields valence changes ΔV of 0.15 ± 0.04 and 0.10 ± 0.01, respectively, for Mn composition
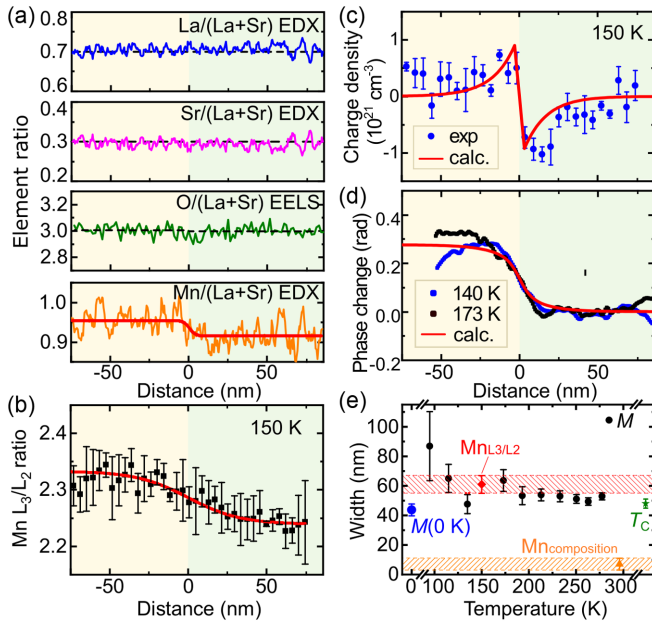
FIG. 4. Chemical composition and electronic properties. (a) Relative La, Sr, O, and Mn composition profiles measured by EDX (La, Sr, Mn) and EELS (O) vs distance. (b) Ratio of integrated Mn-L_3 and L_2 edges measured by EELS vs distance, revealing a change of the Mn valence. The red solid lines in (a) and (b) represent hyperbolic tangent fits. (c) Charge distribution vs distance derived from the measured Mn valence, under consideration of the Mn composition profile in (a). The red solid line represents the theoretical charge distribution for two LSMO layers with different free carrier concentrations calculated using the continuity and Poisson equations. (d) Electrostatic phase shift profiles measured by EH compared to a simulation (red solid line), based on the above electrostatic and the mean inner potential change induced by the Mn composition change. The agreement corroborates the presence of charge redistribution. (e) Temperature dependence of the transition region widths of the magnetization (black circles) compared to that of the Mn valence (red diamond), Mn composition (orange triangle), and T_C (green star).

changes measured using EDX and SIMS, respectively. These values agree with that derived from the L_3/L_2 ratio change, suggesting that ΔV far away from the transition region is governed by the Mn composition difference.

The above valence changes assume that charge neutrality is present. This can be indeed assumed to be the case far away from the interface between the two LSMO sublayers. However, within the transition region, the width of the valence change probed by the Mn L_3/L_2 ratio of 61 ± 6 nm is much wider than the width of the compositional change of Mn of 7 ± 4 nm. Hence, charge neutrality cannot be maintained in the transition region: The charge distribution can be explicitly derived by subtracting the experimentally measured Mn valence distribution [derived from Fig. 4(b)] and the valence distribution expected in case of charge neutrality for the given Mn composition profile

[Fig. 4(a)]. The derived charge distribution in Fig. 4(c) reveals opposite charge densities in both sublayers, reaching $(0.5 - 1) \times 10^{21}$ cm^{-3} at the interface and decaying into both sublayers with a decay length in line with the width of the transition region.

The presence of this charge redistribution can be further corroborated by the measured electrostatic phase shift in EH. Figure 4(d) shows two extracted electrostatic phase shift profiles acquired at 140 and 173 K, which reveal a significant offset and a transition region width in line with a potential change induced by the above derived charge distribution.

Finally, we compare the above derived widths of the magnetic and electrostatic characteristics of the transition region vs temperature in Fig. 4(e). The data reveal, that (i) the width of the transition region exhibits no obvious temperature dependence, (ii) the width of the electrostatic (i.e., valence change, charge distribution) and magnetic (magnetization and T_C) characteristics agree very well, and (iii) both magnetic and electrostatic characteristics have a much wider transition region than the sharp Mn compositional change. The comparison suggests an interplay between magnetic and electrostatic properties.

The question arises, how the magnetic and electrostatic properties are coupled: Free carriers (holes in LSMO) are situated in the density of states (DOS) at the Fermi energy. In LSMO the DOS at the Fermi energy is given by the spin-up e_g state localized at the Mn atoms [32]. Hence, the free holes are localized in the e_g states bound to the Mn atoms and charge transport is mediated by hopping between adjacent Mn^{3+} and Mn^{4+} e_g states [33,34]. Simultaneously, the presence or absence of a free hole in a Mn spin-up e_g state also changes the valence of this particular Mn atom. Thus, the spatial redistribution of free holes corresponds one-to-one with the spatial distribution of the Mn valence [35–37], which in turn determines the magnetization.

For assessing the electrostatic properties, we recall that an increase of the average Mn valence of $\Delta V = +0.136$ decreases the ideal 70% occupation of the e_g state to 56.4%, increasing the free carrier concentration (i.e., holes) [34] from 5×10^{21} (sublayer A) to 7.27×10^{21} cm^{-3} (sublayer B). This yields a composition-induced step in carrier concentration at the interface, which is smoothed by carrier diffusion and drift, in analogy to a p-n junction. The diffusion is counterbalanced by the buildup of an electric field, creating a depletion-zone-like region. We quantitatively modeled this by solving self-consistently the Poisson and continuity equations in the framework of the drift and diffusion model [38,39]. For LSMO the calculated depletion width reaches 40 nm and more, despite high carrier concentrations, since the high permittivity of 3×10^4 [40] is many orders of magnitude larger than in, e.g., silicon. The simulated net charge distribution and electrostatic phase shift agree very well in amplitude and

width with the measured values [compare red line with data in Figs. 4(c), 4(d)]. In addition, the calculated width of the depletion-zone-like region agrees very well with that measured from the L_3/L_2 ratio and from the magnetization at various temperatures [Fig. 4(e)]. This suggests that the origin of the width of the charge and magnetic transitions is the depletion-zone-like region between layers with different carrier concentrations.

The model can be corroborated further by considering the different energy contributions: Using the above simulation, we obtain an electrostatic energy per interface area $w_{ES} = \frac{1}{2} \int \varphi \cdot \rho \, dx = 0.2$ J/m^2, with potential φ and charge density ρ (Ref. [16], p. 4). This value has to be compared to the exchange interaction energy [41] per interface area F approximated by

$$w_{Ex} = \frac{1}{F} \iiint A \left(\frac{\nabla M}{M_S} \right)^2 dV$$

$$= A \int\limits_{-\infty}^{\infty} \left[\frac{\partial}{\partial x} \tanh \left(\frac{1.76x}{w} \right) \right]^2 dx = \frac{4}{3} A \frac{1.76}{w},$$

using a $M_S \cdot \tanh(1.76x/w) + \text{const}$ ansatz for M (see Figs. 2 and 3). Using a width $w = 50$ nm and a stiffness constant A ranging between 1.7 and 5.5 pJ/m [22,42–44], one obtains $w_{Ex} = (0.8–2.6) \times 10^{-4}$ J/m^2, which is 3 orders of magnitude smaller than the electrostatic energy. This demonstrates that the electrostatic energy is largely dominating any magnetic energy contribution.

This is in contrast to classical magnetic DWs, which are governed by the minimization of the total magnetic energy, e.g., mainly exchange interaction and magnetocrystaline anisotropy energies. Although the widths of the classical DWs for perovskite-typeoxide materials, i.e., LSMO ($w = 35.8 \pm 3.2$ nm) [22], La$_{0.7}$Ca$_{0.3}$MnO$_3$ ($w = 38 \pm 10$ nm) [45], and La$_{0.25}$Pr$_{0.375}$Ca$_{0.375}$MnO$_3$ ($w \sim 39$ nm) [46], are similar to ours, the underlying physical mechanisms are fundamentally different. Our magnetic transition region is governed solely by the electrostatics. At this stage we note that changes of interface magnetism induced by application of electrostatic fields [35,47–49], could be driven by an analogous magnetoelectric coupling mechanisms.

In conclusion, we report an experimental example of a magnetic transition region where the magnitude of magnetization gradually changes without rotation. In contrast to the Bulaevskii-Ginsburg DW, which is only stable near T_C, the transition region that we observe persists at all temperature below T_C. This is traced to charge redistribution, caused by the equilibrium between carrier diffusion and drift in the electrostatic field at an interface with a sharp Mn compositional change in LSMO, governing the shape, magnitude, and extent of the corresponding magnetic transition region. The magnetoelectrostatic coupling is mediated by the Mn e_g states' occupation (changing the

Mn^{3+}/Mn^{4+} ratio), which affects both, the magnetization by Mn^{3+}/Mn^{4+} double exchange interaction as well as the free carrier concentration and hence electrostatics. Thus, our results demonstrate a case of the electrostatic shaping of magnetic transition regions. Such electrostatic shaping of magnetic transition regions can be expected to be a general property of complex oxide materials with large permittivity, since the valence and charge carrier concentrations can also be affected by fluctuations in the oxygen composition, in analogy to the change in Mn composition analyzed here.

[*]Corresponding author.
q.lan@fz-juelich.de
[†]Corresponding author.
xzhong25@cityu.edu.hk

[1] A. Hubert and R. Schäfer, *Magnetic Domains: The Analysis of Magnetic Microstructures* (Springer Science & Business Media, Berlin, Heidelberg, New York, 2008).
[2] F. Bloch, Z. Phys. **74**, 295 (1932).
[3] L. Néel, C. R. Hebd. Séances Acad. Sci. **241**, 533 (1955).
[4] M. S. Wörnle, P. Welter, M. Giraldo, T. Lottermoser, M. Fiebig, P. Gambardella, and C. L. Degen, Phys. Rev. B **103**, 094426 (2021).
[5] E. E. Huber, D. O. Smith, and J. B. Goodenough, J. Appl. Phys. **29**, 294 (1958).
[6] S. Middelhoek, J. Appl. Phys. **34**, 1054 (1963).
[7] K. Kuepper, M. Buess, J. Raabe, C. Quitmann, and J. Fassbender, Phys. Rev. Lett. **99**, 167202 (2007).
[8] Y. Yao, B. Ding, J. Liu, J. Liang, H. Li, X. Shen, R. Yu, and W. Wang, arXiv:2201.01406.
[9] G. Chen, J. Zhu, A. Quesada, J. Li, A. T. N'Diaye, Y. Huo, T. P. Ma, Y. Chen, H. Y. Kwon, C. Won, Z. Q. Qiu, A. K. Schmid, and Y. Z. Wu, Phys. Rev. Lett. **110**, 177204 (2013).

[10] G. V. Karnad, F. Freimuth, E. Martinez, R. Lo Conte, G. Gubbiotti, T. Schulz, S. Senz, B. Ocker, Y. Mokrousov, and M. Kläui, Phys. Rev. Lett. **121,** 147203 (2018).

[11] J. Lucassen, M. J. Meijer, F. Kloodt-Twesten, R. Frömter, O. Kurnosikov, R. A. Duine, H. J. M. Swagten, B. Koopmans, and R. Lavrijsen, Phys. Rev. Lett. **123,** 157201 (2019).

[12] R. D. McMichael and M. J. Donahue, IEEE Trans. Magn. **33,** 4167 (1997).

[13] M. Kläui, J. Phys. Condens. Matter **20,** 313001 (2008).

[14] V. D. Nguyen, O. Fruchart, S. Pizzini, J. Vogel, J. C. Toussaint, and N. Rougemaille, Sci. Rep. **5,** 12417 (2015).

[15] L. N. Bulaevskii and V. L. Ginzburg, Sov. Phys. JETP-USSR **18,** 530 (1964).

[16] L. D. Landau and E. Lifshitz, *Electrodynamics of Continuous Media. Course of Theoretical Physics*, 2nd ed., revised and enlarged by E. M. Lifshitz and L. P. Pitaevskii (Pergamon Press, Oxford, 1984), Vol. 8, pp. 152–153.

[17] A. M. Kosevich, B. Ivanov, and A. Kovalev, Phys. Rep. **194,** 117 (1990).

[18] C. Kittel and P. McEuen, *Kittel's Introduction to Solid State Physics* (John Wiley & Sons, New York, 2018), pp. 330–335.

[19] See Supplemental Material at http://link.aps.org/supplemental/10.1103/PhysRevLett.129.057201 for more information on sample preparation, electron holographic tomography to determine the out-of-plane magnetization component, as well as microstructure characterization in LSMO.

[20] M. Huijben, L. W. Martin, Y. H. Chu, M. B. Holcomb, P. Yu, G. Rijnders, D. H. A. Blank, and R. Ramesh, Phys. Rev. B **78,** 094413 (2008).

[21] S. Chen, C. Guan, S. Ke, X. Zeng, C. Huang, S. Hu, F. Yen, H. Huang, Y. Lu, and L. Chen, ACS Appl. Mater. Interfaces **10,** 18029 (2018).

[22] K. J. O'Shea, D. A. MacLaren, D. McGrouther, D. Schwarzbach, M. Jungbauer, S. Hühn, V. Moshnyaga, and R. L. Stamps, Nano Lett. **15,** 5868 (2015).

[23] T. Kasama, M. Beleggia, and R. E. Dunin-Borkowski, *Electron holography of Magnetic Materials* (Intechopen London, United Kingdom, 2011), pp. 57–61.

[24] R. E. Dunin-Borkowski, M. R. McCartney, D. J. Smith, and S. S. P. Parkin, Ultramicroscopy **74,** 61 (1998).

[25] T. Kasama, M. S. Moreno, R. E. Dunin-Borkowski, S. B. Newcomb, N. Haberkorn, J. Guimpel, and P. A. Midgley, Appl. Surf. Sci. **252,** 3977 (2006).

[26] J. Caron, RWTH Aachen University, Ph.D thesis, 2017.

[27] S. McVitie and M. Cushley, Ultramicroscopy **106,** 423 (2006).

[28] F. Bloch, Z. Phys. **61,** 206 (1930).

[29] L. Marín, L. A. Rodriguez, C. Magén, E. Snoeck, R. Arras, I. Lucas, L. Morellón, P. A. Algarabel, J. M. De Teresa, and M. R. Ibarra, Nano Lett. **15,** 492 (2015).

[30] M. Varela, M. P. Oxley, W. Luo, J. Tao, M. Watanabe, A. R. Lupini, S. T. Pantelides, and S. J. Pennycook, Phys. Rev. B, 085117 **79** (2009).

[31] H. Tan, J. Verbeeck, A. Abakumov, and G. Van Tendeloo, Ultramicroscopy **116,** 24 (2012).

[32] S. Yousefi Sarraf, S. Singh, A. C. Garcia-Castro, R. Trappen, N. Mottaghi, G. B. Cabrera, C.-Y. Huang, S. Kumari, G. Bhandari, and A. D. Bristow, ACS Nano **13,** 3457 (2019).

[33] A. J. Millis, Nature (London) **392,** 147 (1998).

[34] M. Cesaria, A. P. Caricato, G. Maruccio, and M. Martino, J. Phys. Conf. Ser. **292,** 012003 (2011).

[35] C. A. F. Vaz, J. Hoffman, C. H. Ahn, and R. Ramesh, Adv. Mater. **22,** 2900 (2010).

[36] C. A. F. Vaz, J. Hoffman, Y. Segal, J. W. Reiner, R. D. Grober, Z. Zhang, C. H. Ahn, and F. J. Walker, Phys. Rev. Lett. **104,** 127202 (2010).

[37] F. Matsukura, Y. Tokura, and H. Ohno, Nat. Nanotechnol. **10,** 209 (2015).

[38] M. Schnedler, V. Portz, P. H. Weidlich, R. E. Dunin-Borkowski, and Ph. Ebert, Phys. Rev. B **91,** 235305 (2015).

[39] M. Schnedler, R. E. Dunin-Borkowski, and Ph. Ebert, Phys. Rev. B **93,** 195444 (2016).

[40] S. Majumdar, H. Huhtinen, P. Paturi, and H. S. Majumdar, J. Mater. Sci. **48,** 2115 (2013).

[41] H. Kronmüller and S. Parkin, *Handbook of Magnetism and Advanced Magnetic Materials* (Wiley, England, 2007), Vol. 2, p. 743.

[42] M. S. Lee, T. A. Wynn, E. Folven, R. V. Chopdekar, A. Scholl, S. T. Retterer, J. K. Grepstad, and Y. Takamura, Phys. Rev. Mater. **1,** 014402 (2017).

[43] S. D. Sloetjes, E. Digernes, F. K. Olsen, R. V. Chopdekar, S. T. Retterer, E. Folven, and J. K. Grepstad, Appl. Phys. Lett. **112,** 042401 (2018).

[44] A. F. Schäffer, L. Chotorlishvili, I. V. Maznichenko, A. Ernst, K. Dörr, I. Mertig, and J. Berakdar, APL Mater. **6,** 076103 (2018).

[45] S. J. Lloyd, N. D. Mathur, J. C. Loudon, and P. A. Midgley, Phys. Rev. B **64,** 172407 (2001).

[46] Y. Murakami, H. Kasai, J. J. Kim, S. Mamishin, D. Shindo, S. Mori, and A. Tonomura, Nat. Nanotechnol. **5,** 37 (2010).

[47] T. Wu, S. B. Ogale, J. E. Garrison, B. Nagaraj, A. Biswas, Z. Chen, R. L. Greene, R. Ramesh, T. Venkatesan, and A. J. Millis, Phys. Rev. Lett. **86,** 5998 (2001).

[48] H. Tanaka, J. Zhang, and T. Kawai, Phys. Rev. Lett. **88,** 027204 (2001).

[49] R. Ramesh and N. A. Spaldin, Nat. Mater. **6,** 21 (2007).